

Full length article

Wear resistance enhancement in Q235 steel via second-scale ultrasonic vibrations

Shike Huang^{a,b,c}, Xiangyang Yu^a, Shengyu Zhao^a, Yihong Yan^a, Jinbiao Huang^a,
Jianyu Chen^a, Sajad Sohrabi^a, Wenqing Ruan^a, Amir Hossein Taghvaei^d, Jiang Ma^{a,b,c,*}

^a State Key Laboratory of Radio Frequency Heterogeneous Integration, Shenzhen University, China

^b Shenzhen Key Laboratory of High Performance Nontraditional Manufacturing, Shenzhen University, Shenzhen 518060, China

^c Guangdong Provincial Key Laboratory of Micro/Nano Optomechatronics, Engineering, Shenzhen University, Shenzhen, China

^d Department of Materials Science and Engineering, Shiraz University of Technology, Shiraz, Iran

ARTICLE INFO

Keywords:

Low-carbon steel
Ultrasonic vibration
Wear resistance
Gradient nanostructure

ABSTRACT

Low-carbon steel is widely used in ships, bridges, and automobiles owing to its combination of plasticity, toughness, and economy. However, its relatively low surface hardness and limited wear resistance fail to satisfy the stringent surface property requirements of advanced manufacturing. Conventional surface modification techniques often suffer from one or more limitations, such as high heat input, weak interfacial bonding, or low processing efficiency, which hinder the long-term stability of surface enhancement. Here, we propose a highly efficient heat-source-free cold manufacturing method. This approach applies high-frequency ultrasonic vibration to the material surface, enabling controllable modulation of its microstructure. For Q235 steel, treatment at 2000 J increases nanohardness from 5.52 to 22.34 GPa, while reducing the wear rate from 13.56×10^{-6} to $3.02 \times 10^{-6} \text{ mm}^3 \text{ N}^{-1} \text{ m}^{-1}$ at room temperature. The process exhibits notable advantages of low stress ($<30 \text{ MPa}$), minimal temperature rise ($\sim 280.6 \text{ }^\circ\text{C}$), and short duration ($<6 \text{ s}$). Moreover, the surface generates a gradient nanostructure about $10 \text{ }\mu\text{m}$ thick, with the grain size refined from $\sim 5 \text{ }\mu\text{m}$ to $\sim 300 \text{ nm}$. Overall, we propose an efficient and economical strategy that is anticipated to enhance the surface properties of steel and other metals by tailoring their microstructure, thereby expanding their practical applications.

1. Introduction

Friction and wear are among the most pervasive failure modes in engineering systems, with wear-induced component damage accounting for a major fraction of equipment failures [1–3]. Moreover, studies indicate that frictional losses account for nearly one-fourth of global energy consumption [4–6]. Therefore, improving the wear resistance of materials is vital for extending service life, enhancing energy efficiency, and reducing maintenance costs [7–10]. Low-carbon steels such as Q235 are widely used in construction, bridges, ships, vehicles, and mechanical components owing to their excellent plasticity, weldability, toughness, and cost-effectiveness [11–13]. However, their inherently low surface hardness and poor wear resistance often lead to plastic deformation and wear failure under frictional contact or heavy loading, thereby limiting their further application in high-end manufacturing, energy equipment, and precision transmission systems [14–17].

To enhance the surface properties of metallic materials, researchers

have proposed and developed various strengthening strategies [18–22]. In general, these approaches can be classified into two categories: one involves constructing a hard surface layer for external strengthening, while the other tailors the internal microstructure to form a gradient structure for internal optimization. Representative techniques of the former include physical vapor deposition (PVD) [23], chemical vapor deposition (CVD) [24], laser cladding [25], thermal spraying [26], carburizing [27], nitriding [28], and carbonitriding [29]. For example, Liu et al. employed laser cladding to produce a Ni-Ti-based gradient coating on $\text{Ti}_6\text{Al}_4\text{V}$, and although the local temperature exceeded $1000 \text{ }^\circ\text{C}$, the process markedly enhanced its wear and corrosion resistance [30]. Yang et al. applied a dual-layer plasma boron-carbon diffusion process to form an Fe_2B boride layer and an Fe_5C_3 transition layer on the surface of Q235 steel, thereby enhancing its high-temperature wear resistance, despite the entire treatment requiring 8 h [31]. Although such methods can significantly enhance hardness and wear resistance, they generally suffer from high thermal energy consumption, complex

* Corresponding author at: State Key Laboratory of Radio Frequency Heterogeneous Integration, Shenzhen University, China.

E-mail address: majiang@szu.edu.cn (J. Ma).

<https://doi.org/10.1016/j.triboint.2026.111887>

Received 16 December 2025; Received in revised form 4 February 2026; Accepted 26 February 2026

Available online 2 March 2026

0301-679X/© 2026 Elsevier Ltd. All rights reserved, including those for text and data mining, AI training, and similar technologies.

processing, and poor coating adhesion [18,23,25,32].

By contrast, gradient structural design introduces a gradual variation in grain size

or microstructural features from the surface to the interior, achieving a synergistic combination of surface hardness and core toughness, and thus emerging as a research focus in recent years [19]. Techniques such as surface mechanical attrition treatment (SMAT) [33], surface mechanical grinding treatment (SMGT) [34], surface mechanical rolling treatment (SMRT) [35], ultrasonic shot peening [36], ultrasonic nanocrystal surface modification (UNSM) [37] and laser shock peening [38] have been widely used to construct gradient nanostructures, enabling a balance between strength and toughness. For instance, Chan et al. generated a high-density nanotwinned structure on the surface layer of 304 stainless steel via surface mechanical treatment, markedly increasing surface hardness while preserving favorable ductility, but the technique suffers from limited controllability [39]. Ren et al. used laser shock processing that generates GPa-level pressure waves to refine the surface grains of Ti₆Al₄V alloy, resulting in a substantial increase in hardness [40]. Lu et al. employed the UNSM technology to induce severe plastic deformation on the material surface through high-frequency impact, thereby achieving grain refinement and enhancing surface hardness; this process typically neither alters the material's chemical composition nor leads to the formation of new species or phases [41]. Overall, existing methods still struggle to achieve the construction of gradient structures in a highly efficient, low-energy, and low-thermal-impact manner [19,20,42]. Thus, developing an efficient, economical, and controllable surface-strengthening strategy with cold-manufacturing characteristics is urgently needed.

In this context, we selected Q235 steel as the research subject and proposed an efficient, heat-source-free strategy for constructing gradient nanostructures. This strategy aims to apply high-frequency ultrasonic vibration (UV) to the material surface to precisely regulate the microstructure of the near-surface layer, thereby generating a gradient nanostructure and significantly enhancing surface hardness and wear resistance. Notably, the nanohardness of Q235 steel increased from 5.52 GPa to 22.34 GPa after treatment with an input energy of 2000 J, while the entire process featured low stress (< 30 MPa), a modest temperature rise (~ 280.6 °C), and an ultrashort processing time (< 6 s). In addition, at room temperature (RT), the wear rate of the sample decreased from 13.56×10^{-6} to 3.02×10^{-6} mm³·N⁻¹·m⁻¹, while the maximum wear depth was reduced from 8.03 μm to 2.67 μm. Meanwhile, the wear mechanism transformed from plastic deformation and adhesive wear to brittle spalling and fatigue wear. Mechanistic analysis reveals that the performance enhancement primarily arises from the synergistic effect between a Fe²⁺/Fe³⁺ composite oxide layer (~1.5 μm in thickness) and a gradient nanostructured layer (~10 μm in depth), both induced to form by UV. In summary, this work provides a new cold-manufacturing approach that is both efficient and economical for enhancing the surface performance of steel and other metallic materials, demonstrating broad potential for engineering applications.

2. Experimental method

2.1. Materials preparation

Q235 steel plates with a thickness of 2 mm were purchased from Dongguan Xinyao Metal Materials Co., Ltd. The plates were first cut into 8 mm × 8 mm square specimens using low-speed wire electrical discharge machining (WEDM; SOD-ICK AP250L). The specimens were then sequentially ground with 800–2000 grit sandpapers and polished with 0.1 μm diamond suspension to achieve a mirror finish, yielding the original Q235 steel samples used for subsequent experiments. Commercial WC balls (9.5 mm diameter) with a hardness of ~15 GPa were purchased from Ningbo Haishu Runchang Cemented Carbide Co., Ltd. and used as counter bodies in the subsequent wear tests.

2.2. Tribological testing

The original and UV-treated Q235 steel samples were subjected to dry sliding wear tests in an air atmosphere at RT using a ball-on-disk tribometer (Rtec MFT-5000, USA). All tests were conducted for 30 min under a load of 50 N, a wear track radius of 4 mm, and a fixed sliding speed of 100 rpm. After testing, all samples were ultrasonically cleaned with alcohol and deionized water to remove surface residues, and the 3D morphology and wear volume of the wear tracks were subsequently evaluated.

2.3. Characterization of multi-scale structures

The microhardness of both the original and treated Q235 steel samples was measured using a Vickers microhardness tester (FM-16 ARS9000, FUTURE-TECH, Japan) under a static load of 120 gf and a dwell time of 12 s. Furthermore, the surface hardness and modulus of the samples were evaluated using a nanoindenter (TI950, Hysitron). The surface morphology and volume loss of the samples after wear testing were analyzed using a white light interferometer (Bruker Contour GT-X 3D). All samples were further characterized for their surface morphology and elemental distribution using a field-emission scanning electron microscope (SEM; FEI QUANTA FEG 450). The surface elemental composition and chemical states of the samples were further analyzed using X-ray photoelectron spectroscopy (XPS; Thermo Scientific, USA) with an Al Kα X-ray source (photon energy: 1.4867 keV). The XPS spectra were calibrated with reference to the C 1 s peak at 284.8 eV, and the characteristic peaks were analyzed using Avantage 6.6 software. Phase constitutions of the samples were identified using an X-ray diffraction (XRD, Rigaku MiniFlex 600) at a scanning rate of 2 °/min over a 2θ range of 10° to 90°. Grain orientation across the sample cross-sections was characterized by electron backscatter diffraction (EBSD; Nordlys Max3, Oxford Instruments, UK) with a step size of 100 nm, and subsequently inverse pole figure (IPF), phase distributions, grain size distributions, kernel average misorientation (KAM) maps, and pole figures were obtained using AZtecCrystal software. Atomic structures on the cross-sections of the ultrasonically treated samples were analyzed using transmission electron microscopy (TEM; JEM-2100F, JEOL Ltd.), and TEM samples were prepared using an FEI Scios SEM/FIB dual-beam system.

3. Results and discussion

3.1. Effect of ultrasonic vibration treatment on surface mechanical properties

The experimental procedure employed in this study is schematically illustrated in Fig. 1(a). The Q235 steel samples were first subjected to UV treatment, followed by wear testing. As can be seen, the square ultrasonic horn contacts the surface of Q235 steel under a certain pressure and applies vibration at a frequency of 20 kHz. Notably, UNSM employs a hard spherical tip in a small-area point-contact mode and scans along a predefined path [43], whereas this method acts on the surface via surface contact, leading to a markedly higher processing efficiency. After ultrasonic treatment, the samples were subjected to ball-on-disk wear tests using WC balls as the counterbodies. The dark-gray regions visible on the surface of the treated sample represent areas where UV influenced the material to a certain depth. Microhardness tests were performed on the original Q235 steel samples and those treated with UV at different energies, using a 3 × 3 array with 1 mm spacing, and the results are shown in Fig. 1(b). It is evident that the microhardness of the sample increases progressively with increasing ultrasonic energy. The average microhardness values of the original sample and those treated with ultrasonic energies of 250, 500, 1000, and 2000 J were 168.7, 299.8, 359.3, 467.3, and 469.9 HV, respectively. For the following reasons, subsequent investigations in this study primarily focus on the samples

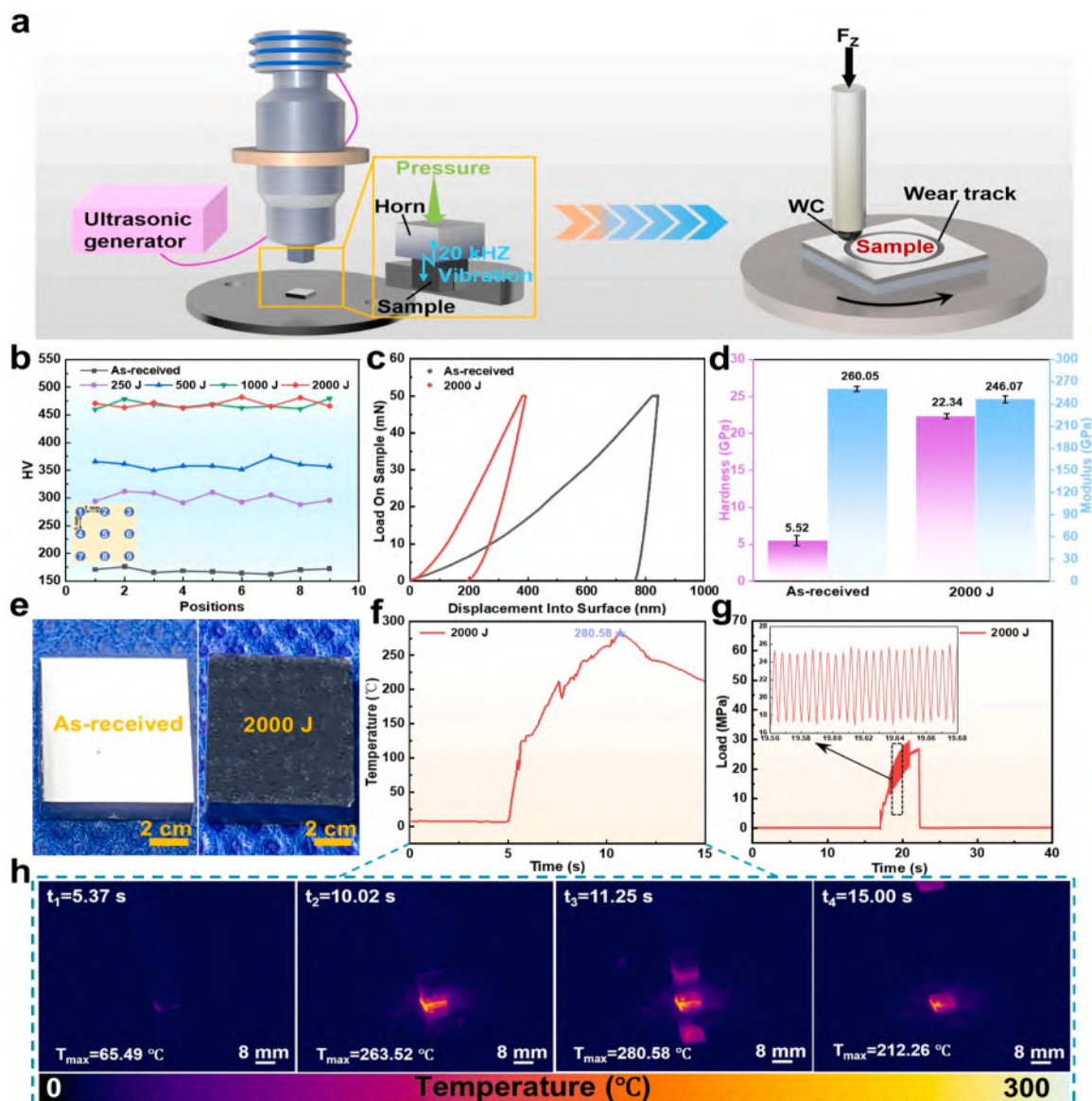


Fig. 1. (a) The schematic diagram of the UV treatment and wear experiment. (b) Comparison of the surface microhardness of Q235 steel after UV at different energies with the original sample. (c-e) The load-displacement curves, nanoindentation hardness and modulus, and optical images of Q235 steel before and after UV treatment at an input energy of 2000 J. (f-g) The surface temperature and load curves of Q235 steel treated by UV with an energy of 2000 J. (h) Thermal infrared images acquired during UV processing of Q235 steel at an energy of 2000 J.

treated at 2000 J. First, the samples processed at 2000 J exhibit slightly higher microhardness than those treated at 1000 J. Second, higher input energy results in a deeper affected layer and potentially extended service life. Finally, excessively high energy may induce severe plastic deformation, accompanied by increased surface roughness, the accumulation of microcracks, or even catastrophic fracture.

Fig. 1(c) shows the load-displacement curve obtained through nanoindentation testing. The samples treated at 2000 J exhibit a markedly smaller indentation depth than the original samples. The surface hardness of the sample increased substantially from 5.52 GPa in the original state to 22.34 GPa after treatment, whereas the surface modulus decreased slightly from 260.05 GPa to 246.07 GPa, as illustrated in Fig. 1(d). Increased hardness may be associated with the formation of new surface species and phases, as well as pronounced microstructural refinement. A slight reduction in modulus may be related to the presence of microstructural defects (such as intergranular gaps), compositional heterogeneity, and the intrinsic structural characteristics of the surface layer. Given that wear resistance is generally

positively correlated with surface hardness [44], it can be inferred that the samples subjected to 2000 J UV treatment exhibited a certain improvement in wear resistance. Fig. 1(e) shows optical images of the Q235 steel samples before and after the 2000 J UV treatment. It can be observed that the surface of the treated sample darkened noticeably and exhibited a certain degree of plastic deformation.

The thermal infrared image captured during the 2000 J UV treatment is presented in Fig. 1(h). Specifically, t_1 , t_2 , t_3 , and t_4 correspond to the stages of initial contact between the horn and the sample surface, near the completion of processing, immediately after separation, and shortly after the process had concluded, respectively. The corresponding maximum temperatures (T_{max}) were 65.49 °C, 263.52 °C, 280.58 °C, and 212.26 °C, respectively. Additionally, the T_{max} and load data recorded throughout the entire UV process were extracted and plotted as curves, as shown in Fig. 1(f) and (g). It can be seen that the 2000 J UV treatment lasted less than 6 s, with a T_{max} of 280.58 °C and a peak load below 30 MPa. In a striking contrast to conventional methods, this process operates with a markedly shorter duration than carburizing [27] or

coating deposition (hours) [23], a temperature rise well below that of laser cladding ($>1000\text{ }^{\circ}\text{C}$) [30] or the phase-transition point of Q235 steel ($>700\text{ }^{\circ}\text{C}$) [45], and an applied load far lower than the GPa-level stresses typical of laser shock peening [40] and UNSM [37]. The inset in Fig. 1(g) distinctly illustrates the rapid periodic fluctuations of the load under UV.

To examine whether UV treatment enhances surface oxidation and thereby contributes to the surface darkening observed after the 2000 J treatment, thermal oxidation experiments were conducted at the same temperature ($280\text{ }^{\circ}\text{C}$) for comparison. As shown in the insets of Fig. 2(a-d), at $280\text{ }^{\circ}\text{C}$ the sample surfaces gradually change from metallic silver to yellow and purple after thermal oxidation for 6 s, 1 min, and 3 min, in contrast to the dark grayish-blue appearance observed after the 2000 J ultrasonic vibration treatment. Meanwhile, the corresponding EDS results indicate that the surface oxygen contents of the samples are approximately 4%, 5%, 8%, and 31%, respectively. These results indicate that UV treatment promotes surface oxidation more effectively than

thermal oxidation alone.

In summary, these results demonstrate that the UV technique employed in this study offers the distinct advantages of rapid processing, low load, and low temperature rise, while significantly enhancing the surface hardness of Q235 steel and promoting surface oxidation.

3.2. Wear behavior and surface morphological analysis

To directly investigate the influence of UV on wear resistance, ball-on-disk wear tests were performed at RT on both original Q235 steel and samples treated with UV at different energies. Fig. 3(a), (c), and (e) present 3D morphologies of the wear tracks on the original sample and those treated with 500 J and 2000 J UV. With increasing ultrasonic energy, the wear tracks gradually became narrower and shallower, accompanied by a slight increase in surface roughness. Compared with the 500 J sample, the original sample exhibited pronounced plastic edge upwarping during wear, whereas no such feature was observed on the

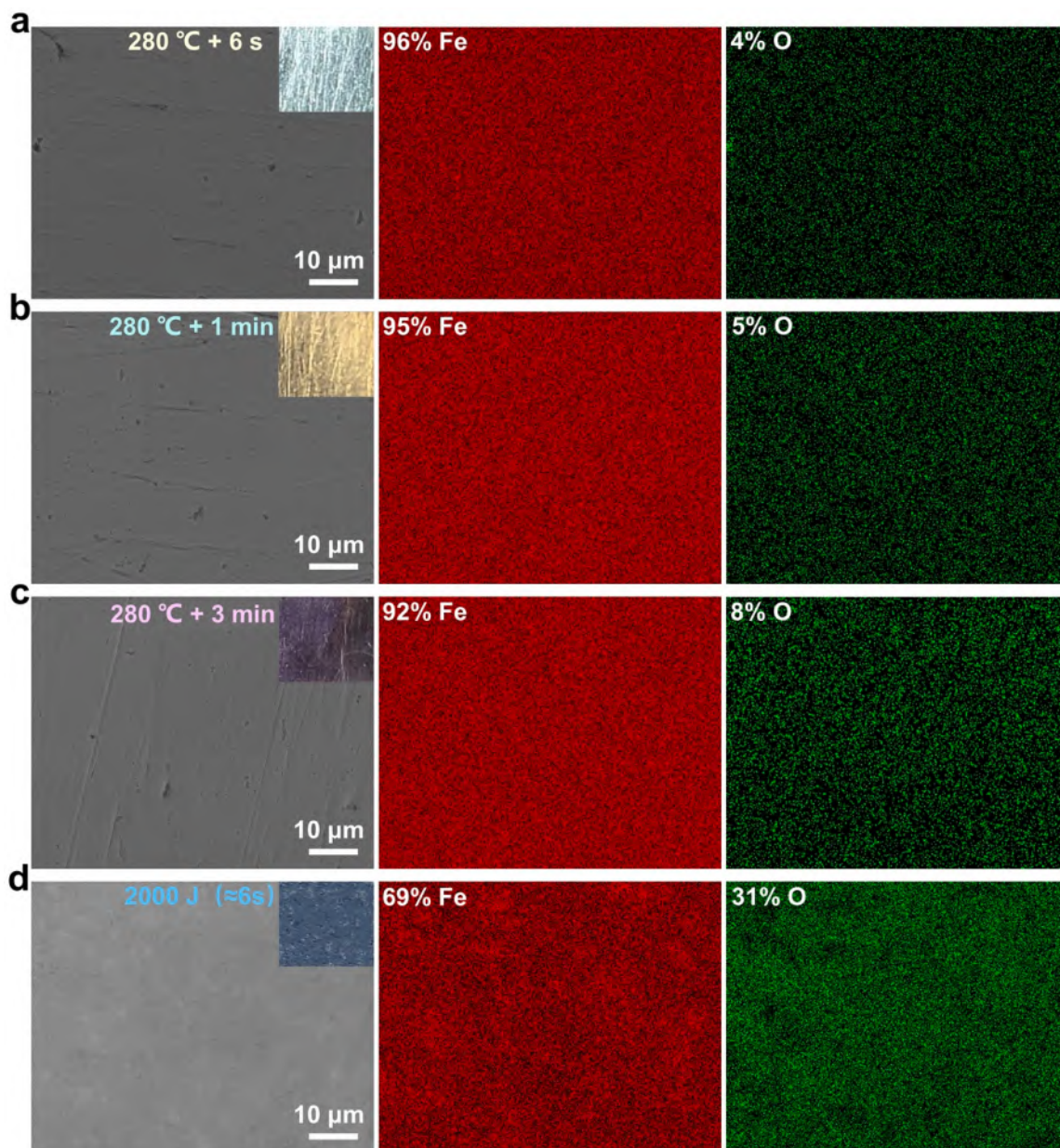


Fig. 2. (a-c) SEM morphologies and optical images of Q235 steel surfaces after thermal oxidation at $280\text{ }^{\circ}\text{C}$ for 6 s, 1 min, and 3 min, along with the corresponding EDS analyses. (d) SEM morphologies and optical images of Q235 steel surfaces after UV treatment at 2000 J, together with the corresponding EDS results.

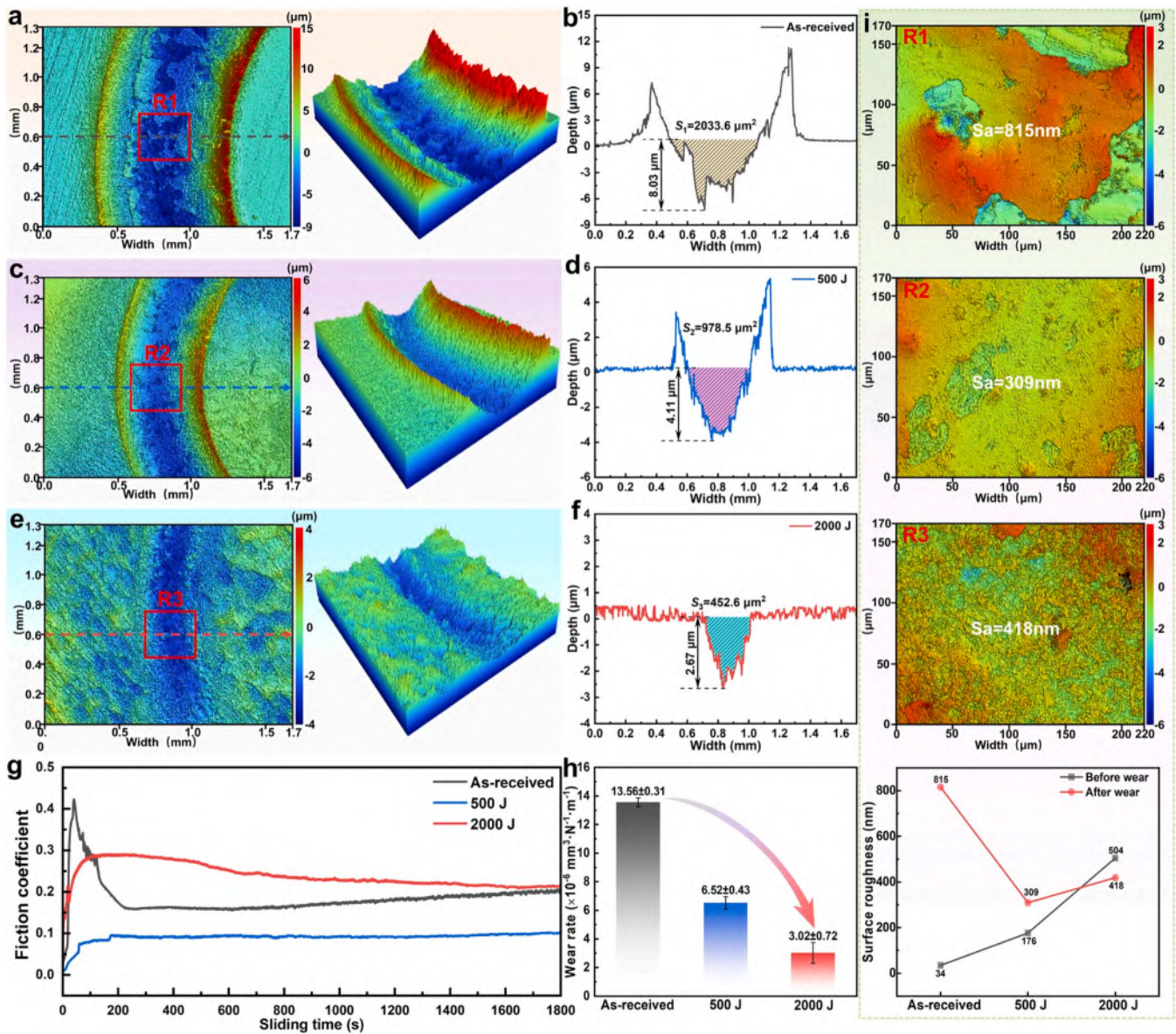


Fig. 3. (a-b) 3D wear surface morphologies and corresponding cross-sectional profiles of the original Q235 steel. (c-d) 3D wear surface morphologies and cross-sectional profiles of the sample treated with UV at 500 J. (e-f) 3D wear surface morphologies and cross-sectional profiles of the sample treated with UV at 2000 J. (g) Coefficient-of-friction curves of the original, 500 J-treated, and 2000 J-treated samples as a function of time. (h) Comparison of wear rates of samples treated with different UV energies. (i) Surface roughness of regions R1, R2, and R3 before and after wear.

2000 J sample after wear. From the cross-sectional profiles, the maximum depths of the wear tracks for the original, 500 J, and 2000 J samples were determined to be 8.03 μm , 4.11 μm , and 2.67 μm , respectively, as shown in Fig. 3(b), (d), and (f). The area of the wear profile is 2033.6 μm^2 (S_1) for the original sample, 978.5 μm^2 (S_2) for the 500 J treated sample, and 452.6 μm^2 (S_3) for the 2000 J treated sample by using the integral method [46].

The three curves in Fig. 3(g) represent the time-dependent coefficients of friction (COF) at RT for the original sample (gray), the 500 J-treated sample (blue), and the 2000 J-treated sample (red), respectively. At the initial stage, the COF for all three samples increased rapidly and then gradually stabilized. To further elucidate the evolution of the COF curves, the surface roughness (S_a) of regions R1, R2, and R3 was quantitatively analyzed before and after wear. As shown in Fig. 3(i), the S_a of regions R1, R2, and R3 after wear increased from 34 nm to 815 nm, increased from 176 nm to 309 nm, and decreased from 504 nm to 418 nm, respectively. Among these regions, R1 exhibits the most

pronounced change in S_a , with numerous deep pits observed in the 3D morphology shown in Fig. 3(a). Owing to the as-received sample's relatively high plasticity and low hardness, it undergoes compressive deformation induced by the WC ball during the initial stage of sliding, resulting in pronounced plastic deformation with limited material removal. As the surface layer is progressively disrupted, the friction process gradually transitions into a wear-dominated stage. This process coincides with the experimentally observed transition from an initially sharp friction noise to a more stable sliding sound. It helps explain the rapid decrease in the COF from an initial value of ~ 0.42 (the highest among the three samples) to ~ 0.16 , followed by a gradual increase to approximately 0.20 at 1800 s. Because the S_a of region R2 before wear lies between that of R1 and R3, and the 500 J UV treatment induces a certain degree of surface oxidation accompanied by increased hardness, the initial COF is approximately 0.097 (the lowest among the three samples). Furthermore, since the S_a of the R2 region increased only slightly after wear, its COF subsequently rose marginally and remained

stable at ~ 0.10 . Region R3 exhibits the highest Sa before wear, and the surface hardness is further increased after the 2000 J UV treatment, resulting in an initial COF of 0.29, which is higher than that of the 500 J sample but lower than that of the as-received sample. Furthermore, as the Sa of region R3 decreases after wear, the COF decreases continuously during sliding and ultimately stabilizes at ~ 0.21 . These results indicate that UV treatment can effectively reduce the COF overall. Although the hardened layer at 2000 J may be deeper, increased surface roughness and oxide film hardness resulted in a higher COF than the 500 J sample. To further quantify the wear resistance, the wear rate of the samples was calculated according to the following Eq. (1):

$$\omega = \frac{V_{\text{loss}}}{L * F} \quad (1)$$

Here, V_{loss} denotes the total wear volume (mm^3), L represents the sliding distance (m), and F refers to the applied normal load (N) [47]. As shown in Fig. 3(h), the wear rates calculated from Eq. (1) were 13.56 , 6.52 , and $3.02 \times 10^{-6} \text{ mm}^3 \text{ N}^{-1} \text{ m}^{-1}$ for the original, 500 J, and 2000 J samples, respectively. UV treatment at 2000 J increased the wear resistance of the sample to approximately 4.5 times that of the original one, demonstrating that this technique can substantially improve the wear resistance of Q235 steel. Moreover, this approach offers a promising and efficient pathway operating under low-load and low-temperature-rise conditions to enhance the wear resistance of other steels and metallic materials.

Fig. 4(a) compares the surface SEM morphologies of Q235 steel in the original and 2000 J treated states before the wear test. The surface of

the treated sample shows a corrugated and pit-rich morphology due to plastic deformation, in contrast to the smooth and flat surface of the original one. As shown in Fig. 4(b) and (c), the surface of the sample treated at 2000 J is covered by a black layer approximately $1.37 \mu\text{m}$ thick. The energy-dispersive spectroscopy (EDS) results at positions P_1 and P_2 (Table 1) show oxygen contents of 47.18% and 11.96%, respectively, indicating that the black layer consists of iron oxides. Fig. 4(d) presents the SEM morphology of the wear track on the original sample, where a clear boundary separates the worn and unworn regions. The worn surface exhibits extensive layered deposits accompanied by warping and groove features. High-magnification images in Fig. 4(e) and (f) show that as sliding wear progresses, the surface experiences extensive peeling and pronounced plastic deformation, with grooves of varying depths distributed across the exposed substrate. Moreover, the presence of small wear debris suggests that abrasive wear also occurs throughout the process. In contrast, the sample subjected to 2000 J UV treatment exhibits distinctly different morphological features, as shown in Fig. 4(g-i). The wear track becomes narrower with shallower grooves, while the extent of surface peeling is markedly reduced. High-magnification SEM image (Fig. 4(i)) reveals abundant brittle spalling pits, indicating that the wear mechanism evolves from plastic deformation to brittle spallation. This transition is closely associated with surface hardening and microstructural refinement induced by UV treatment. Further inspection of Fig. 3(f) shows that the maximum wear track depth ($\sim 2.67 \mu\text{m}$) exceeds the oxide layer thickness ($\sim 1.37 \mu\text{m}$), indicating that the WC counterbody has penetrated the oxide layer and entered direct contact with the substrate. Correspondingly, the SEM

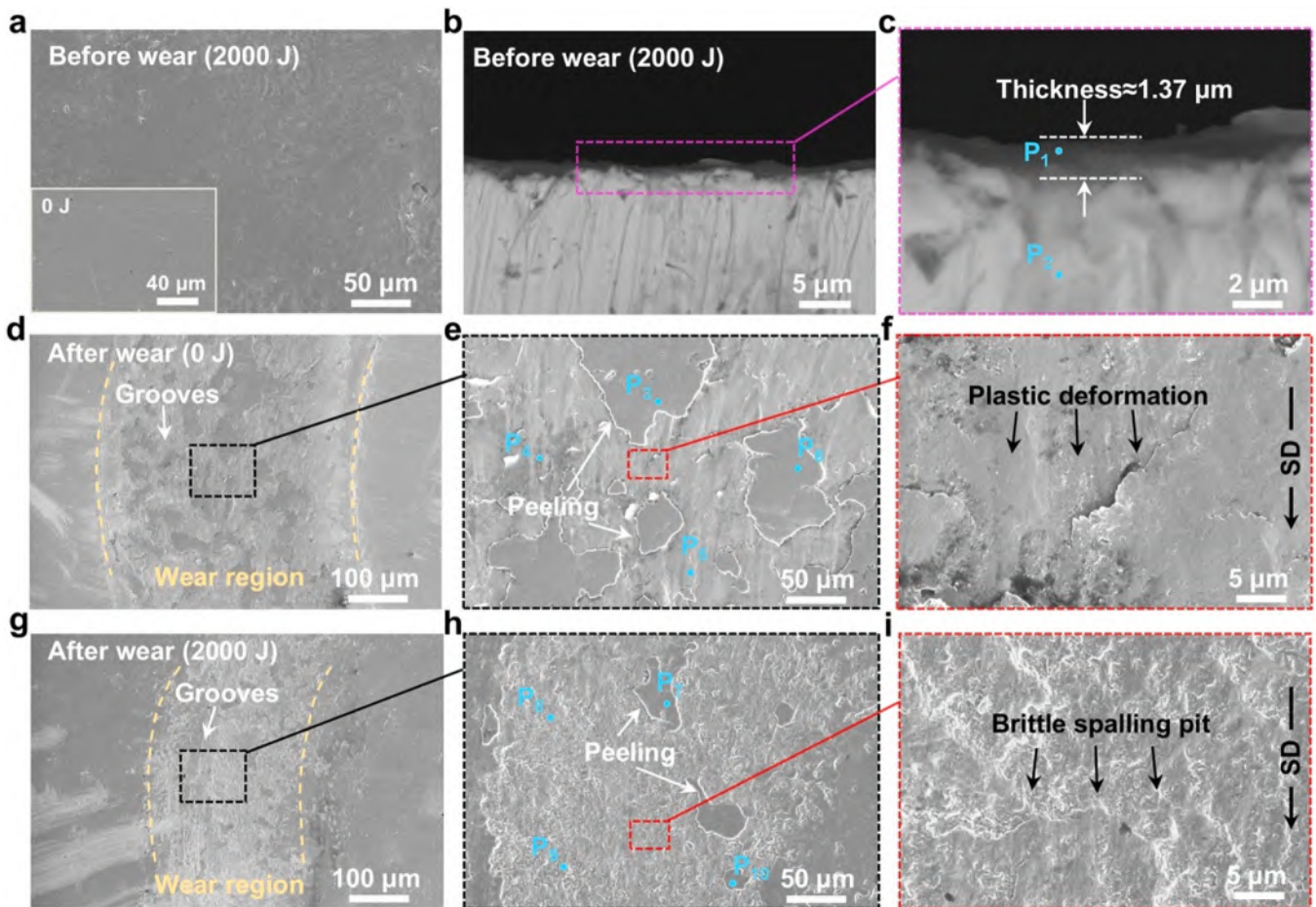


Fig. 4. (a) SEM images of the original Q235 steel and the sample treated with 2000 J UV before wear testing. (b-c) The cross-sectional morphology of the sample after 2000 J UV treatment was observed at different magnifications. (d-e) SEM morphologies of the worn surfaces of the original Q235 steel at different magnifications. (g-i) SEM morphologies of the worn surfaces of the 2000 J UV-treated Q235 steel at varying magnifications.

Table 1

Summary of elemental distribution in the wear tracks of Q235 steel before and after 2000 J UV treatment.

Point (No.)	Element content (at%)									
	O	Fe	Si	Mn	C	Ni	Cr	S	P	W
P ₁	47.18	50.22	2.14	0.07	0.17	0.06	0.1	0.04	0.01	0.01
P ₂	11.96	86.73	0.37	0.56	0.01	0.13	0.21	0.01	0.01	0.01
P ₃	46.21	51.28	1.87	0.23	0.01	0.24	0.08	0.06	0.01	0.01
P ₄	6.84	92.12	0.46	0.24	0.02	0.13	0.12	0.05	0.01	0.01
P ₅	45.26	52.61	1.63	0.20	0.02	0.13	0.12	0.01	0.01	0.01
P ₆	9.62	89.48	0.28	0.31	0.02	0.12	0.13	0.02	0.01	0.01
P ₇	49.64	47.82	1.92	0.33	0.10	0.08	0.07	0.02	0.01	0.01
P ₈	21.18	76.96	0.93	0.47	0.04	0.17	0.17	0.06	0.01	0.01
P ₉	20.54	76.79	0.92	0.65	0.23	0.38	0.32	0.15	0.01	0.01
P ₁₀	44.42	54.22	0.45	0.52	0.01	0.11	0.24	0.01	0.01	0.01

images reveal characteristic wear features of the substrate. Moreover, the worn debris generated by brittle spallation in this region is similar to conventional debris and may further exacerbate the wear process to some extent.

Further EDS analyses were performed at positions P₃, P₄, P₅, P₆, P₇, P₈, P₉, and P₁₀, and the corresponding results are summarized in Table 1. The oxygen contents in the peeling regions corresponding to positions P₃, P₅, P₇, and P₁₀ are 46.21%, 45.26%, 49.64%, and 44.42%, respectively, indicating that these areas are composed of oxides formed during wear and that oxidative wear occurred in the process. At the exposed substrate positions P₄, P₆, P₈, and P₉, the oxygen contents are 6.84%, 9.62%, 21.18%, and 20.54%, respectively, suggesting that the heat generated during wear induced partial oxidation of the substrate. The higher oxygen content in the treated samples is attributed to initial oxidation caused by the temperature rise during UV treatment. The W content on the surfaces of these samples is only 0.01%, indicating that no significant adhesion of the counterbody to the sample surface occurred. Other trace elements are inherent constituents of Q235 steel and therefore not discussed further here. Furthermore, the principal element in Q235 steel exhibits an inverse complementary relationship with oxygen. For instance, an increase in oxygen content corresponds to a decrease in iron content.

Distinct wear morphologies are observed for the WC balls after wear

tests against different samples. Fig. 5(a-c) presents the SEM morphologies of the WC balls after sliding against the as-received Q235 steel sample, together with the corresponding EDS results. The WC ball experiences relatively mild self-wear under this condition. Its surface is covered with abundant large flake-like and densely aggregated particulate oxides generated from the as-received Q235 steel sample during sliding, indicating a pronounced transfer of the oxide layer formed on the steel surface. This further suggests that strong adhesive interactions occur during sliding, which is likely related to the high surface plasticity of the as-received Q235 steel sample. In contrast, sliding against the 2000 J treated Q235 steel results in more pronounced wear of the WC ball, with its surface mainly decorated by a limited amount of small flake-like debris and abundant dispersed particulate matter, as shown in Fig. 5(d) and (f). The EDS results in Fig. 5(e) further indicate that the flake-like and particulate materials adhering to the WC ball surface originate from the transfer of the oxide layer on the sample surface. These features indicate that the friction process is dominated by brittle spalling, which is closely associated with the pronounced increase in surface hardness and brittleness after the 2000 J treatment. The transfer film formed in both cases reduces the direct contact between the WC ball and the sample surface to some extent and promotes a transition of the friction process toward a more stable and mild wear state.

Overall, under wear conditions of 50 N and 100 rpm, the original

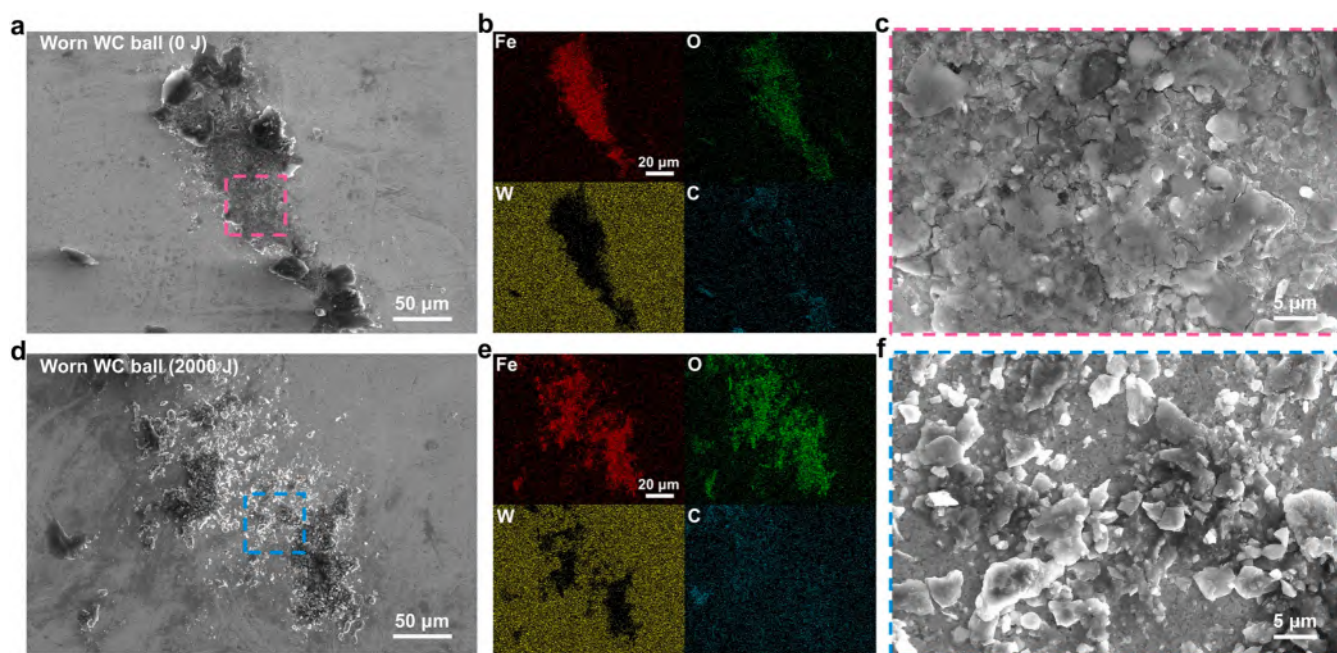


Fig. 5. (a-b) SEM morphologies and corresponding EDS results of the WC balls after sliding against the as-received Q235 steel. (c) High-magnification SEM morphology of the area marked by the pink frame in (a). (d-e) SEM morphologies and corresponding EDS results of the WC balls after sliding against the Q235 steel treated by 2000 J UV. (f) High-magnification SEM morphology of the area marked by the blue frame in (d).

Q235 steel underwent pronounced plastic deformation. Its wear mechanism was dominated by adhesive wear and supplemented by oxidative, abrasive, and fatigue wear. In contrast, the samples treated with 2000 J UV exhibited wear behavior predominantly characterized by brittle spallation and fatigue wear, with minor involvement of oxidative, abrasive, and adhesive wear.

3.3. Surface chemical states and phase composition

Both the original and treated samples were characterized using XPS to investigate the reason for the enhanced wear resistance. Fig. 6(a) shows the Fe 2p spectrum of the original Q235 steel sample. The Fe 2p spectrum exhibits two distinct peaks located at 706.58 eV and 710.32 eV, which are attributed to Fe and Fe₃O₄, respectively, accounting for 11.96% and 88.04%. Fig. 6(b) shows the O 1s spectrum of the original Q235 steel sample, where Fe–O (529.73 eV), C=O (531.25 eV), and C–O (532.25 eV) peaks can be observed, with proportions of 48.77%, 28.31%, and 22.92%, respectively. These results demonstrate that the surface of the original Q235 steel sample contains Fe₃O₄ along with minor organic carbon oxides. Fig. 6(c) presents the Fe 2p spectrum of the Q235 steel sample subjected to 2000 J UV treatment. It can be seen that the spectrum is mainly composed of two peaks located at 709.09 eV and 711.13 eV, corresponding to Fe (II)–O and Fe (III)–O [48], with proportions of 44.14% and 55.86%, respectively. Unlike the original sample, where Fe is present in a mixed-valence form (Fe₃O₄),

the sample treated with 2000 J UV exhibits Fe²⁺ and Fe³⁺ species as independent oxidation states. This indicates that UV promotes oxidation and alters the valence-state distribution of iron. Fig. 6(d) shows the O 1s spectrum of the treated sample. The spectrum consists of three components corresponding to M–O (529.93 eV), C=O (531.89 eV) and C–O (533.48 eV) bonds, with proportions of 69.69%, 22.45% and 7.86%, respectively. Compared with the original sample, the M–O component increases markedly, whereas the C=O and C–O components decrease significantly, indicating that UV treatment promotes metal oxidation and strengthens the formation of metal–oxygen bonds. These results further verify that UV enhances the oxidation effect during the treatment process.

According to the XRD results in Fig. 7, the Fe₃O₄ layer on the surface of the original sample is only several tens of nanometers thick, and the substrate is primarily composed of Fe (110), (200), and (211) crystal planes. The substrate of the treated sample retains the same crystal planes, but distinct diffraction peaks of Fe₂O₃ and Fe₃O₄ appear on the surface, consistent with the XPS results. It can be concluded that UV treatment leads to the formation of a high-hardness iron oxide layer on the sample surface, composed of coexisting Fe²⁺ and Fe³⁺, which provides the basis for its markedly enhanced wear resistance.

3.4. Microstructural changes induced by ultrasonic vibration treatment

As the microstructure exerts a substantial influence on the wear

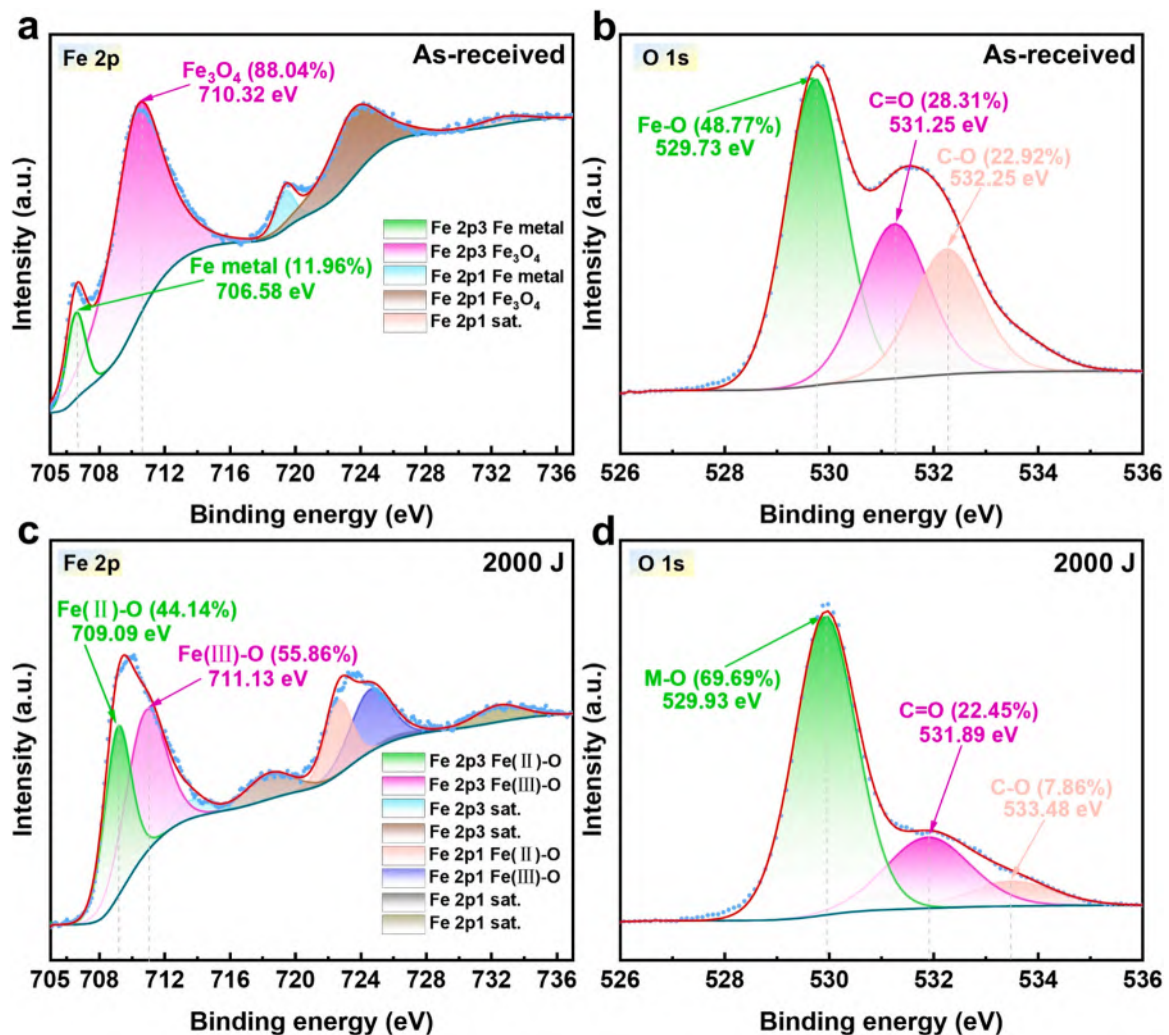


Fig. 6. (a-b) XPS spectra of Fe 2p and O 1s on the surface of the original Q235 steel. (c-d) XPS spectra of Fe 2p and O 1s on the surface of Q235 steel after 2000 J UV treatment.

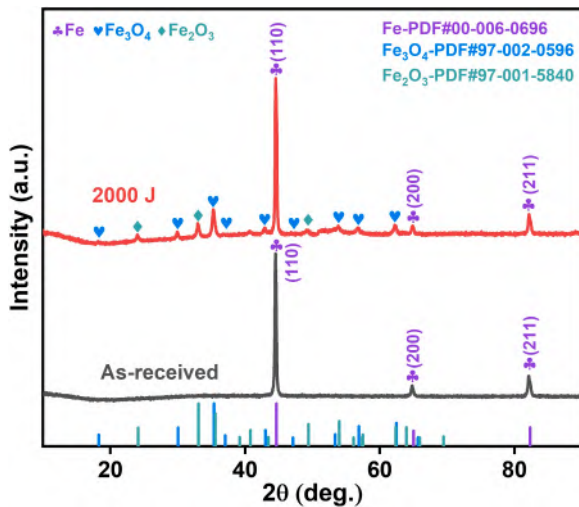


Fig. 7. XRD patterns of Q235 steel before and after UV at an energy of 2000 J.

resistance of materials [49], it was subjected to systematic characterization and analysis. Owing to the low fraction of the β -Fe phase in Q235 steel, the α -Fe phase was adopted as the reference for EBSD analysis. Fig. 8(a-c) present the IPF orientation, phase, and grain size distribution maps of the cross-section of the original Q235 steel sample, respectively. It can be observed that the sample exhibits a polygonal equiaxed microstructure with a body-centered cubic (BCC) crystal structure. The grains show a certain degree of orientation anisotropy, consistent with the XRD results, and the average grain size is approximately 5 μm . Fig. 8(d) shows the KAM map of the original sample, where blue and green regions correspond to low and high dislocation densities, respectively, indicating that the overall dislocation density of the original sample is relatively low. The pole figure in Fig. 8(e) displays the orientation distributions for the (100), (110), and (111) crystallographic planes of the original sample. It is evident that the pole distributions are predominantly diffuse, with only weak localized orientation concentrations, and the maximum orientation intensity reaches 8.36. These observations indicate a weak overall texture with largely random grain orientations and no discernible preferred orientation, consistent with a typical polycrystalline equiaxed ferritic microstructure.

In contrast, the samples subjected to 2000 J UV treatment retained the BCC crystal structure but exhibited significant and uniform grain refinement, as shown in Fig. 8(f-h). The most pronounced grain-refined layer is approximately 10 μm thick, with an average grain size of \sim 545 nm, where grains around 300 nm are the most numerous. This provides a strong rationale for the sample to have better wear resistance than the as-received Q235 steel, even after the oxide layer has worn away. Fig. 8(i) shows that the treated sample exhibits a higher dislocation density, indicating that UV induces intense plastic deformation and dislocation accumulation. Fig. 8(j) presents the pole figures of the treated sample, showing that the pole distributions of the (100), (110), and (111) planes transform from a diffuse state to locally concentrated regions. Distinct orientation strengthening is observed in certain areas, with the maximum pole intensity reaching 11.86. These results demonstrate that high-energy UV induces grain reorientation and texture strengthening while simultaneously promoting grain refinement and dislocation activity. Collectively, this microstructural evolution establishes a basis for the substantial improvements in mechanical and wear performance.

To further investigate the microstructural evolution, the sample subjected to the 2000 J UV treatment was characterized and analyzed using TEM. As shown in Fig. 9(a), the cross-sectional TEM image reveals that the grain size gradually increases from the surface toward the core of the sample. Based on the EDS results shown in Fig. 9(b), the surface

layer of the sample is identified as a compact Fe-containing oxide with a thickness of approximately 1.5 μm . By contrast, the indentation depth in the nanoindentation test is approximately 200 nm (Fig. 1(c)), which is far smaller than the oxide layer thickness, indicating that the indentation response is dominated by the oxide layer itself. In the remaining regions, the elemental distribution appears uniform, with no evident elemental segregation observed. Fig. 9(c-e) presents high-magnification TEM images of the regions labeled R1, R2, and R3, with corresponding average grain sizes of approximately 20.36 nm, 31.54 nm, and 60.42 nm, respectively. A distinct boundary is observed in the R3 region, where the grains near the core exceed 130 nm in size.

Numerous studies have demonstrated that nanocrystalline materials containing ultrafine grains and a high density of grain boundaries can provide fast atomic diffusion pathways, leading to a markedly enhanced atomic diffusion rate [50–58]. Accordingly, it is reasonable to infer that the pronounced grain refinement induced by UV in this work provides effective diffusion pathways for O or Fe atoms, thereby facilitating the oxidation process. Molecular dynamics simulations were further employed to investigate the mobility of Fe atoms. As shown in Fig. 10(a), the mean square displacement (MSD) of Fe atoms in the 2000 J UV treated sample reaches \sim 0.63 \AA^2 , which is markedly higher than that of the sample subjected to thermal treatment at 280 $^{\circ}\text{C}$ (\sim 0.06 \AA^2). As shown in Fig. 10(b), under thermal treatment at 280 $^{\circ}\text{C}$, the displacement r of an individual Fe atom remains stable at approximately 0.3 \AA over the time interval from 300 to 900 ps. By contrast, in the 2000 J UV treated sample, the displacement r of an individual Fe atom increases from approximately 1 \AA at 300 ps to 3.3–4 \AA at 900 ps, indicating an accelerated atomic migration rate. Thus, the enhanced oxidation induced by UV arises from a synergistic mechanism: UV activates Fe atomic mobility, while the associated grain refinement and high density of grain boundaries provide rapid diffusion pathways for O or Fe atoms. Benefiting from this synergistic mechanism, the Q235 steel treated by 2000 J UV ultimately formed an oxide layer with micrometre-scale thickness, which is substantially thicker than the nanometre-scale oxide layers formed under conventional short-time thermal oxidation conditions.

Fig. 9(f-h) shows the high-resolution TEM images of the purple-marked regions and their corresponding fast fourier transform (FFT) patterns. It can be observed that the atomic spacings in the three regions are 0.116 nm, 0.145 nm, and 0.192 nm, respectively. With increasing depth, the atomic structure evolves from a disordered amorphous surface with minor crystalline domains, via a crystallinity-dominated mixed state containing limited amorphous regions, to a fully crystalline structure. The FFT patterns in the insets also demonstrate this evolution: the diffraction halos progressively disappear, diffraction spots increase in number and sharpen, and ultimately only well-defined spots remain. The selected-area electron diffraction (SAED) results further reveal that region R4 corresponds to the (222) and (422) planes of Fe_3O_4 and the (024) plane of Fe_2O_3 , as shown in Fig. 9(i). By comparison, Fig. 9(j) reveals that region R5 retains the (222) and (422) planes of Fe_3O_4 , while the Fe_2O_3 plane transforms to (214). Fig. 9(k) shows that region R6 is primarily composed of the (211) and (110) planes of Fe. The TEM results are consistent with the XPS and XRD analyses, further confirming that the 2000 J UV treatment induces the formation of a composite oxide layer containing both Fe^{2+} and Fe^{3+} on the sample surface. By combining the TEM and EBSD analyses, it can be confirmed that the treated sample develops a gradient nanostructure in the surface layer with a thickness of approximately 10 μm . It can be concluded that the formation of gradient nanostructures and Fe-rich oxide layers constitutes the critical microscopic mechanism to significantly enhance the surface hardness and wear resistance of the samples. Based on all the results presented above, it can be inferred that the oxide layer (\sim 22 GPa) of the sample exhibits a nanoindentation hardness far exceeding that of conventional nanocrystalline iron (\sim 10 GPa), owing to the synergistic effects of multiple factors: pronounced microstructural refinement, the formation of new species and phases, and the presence

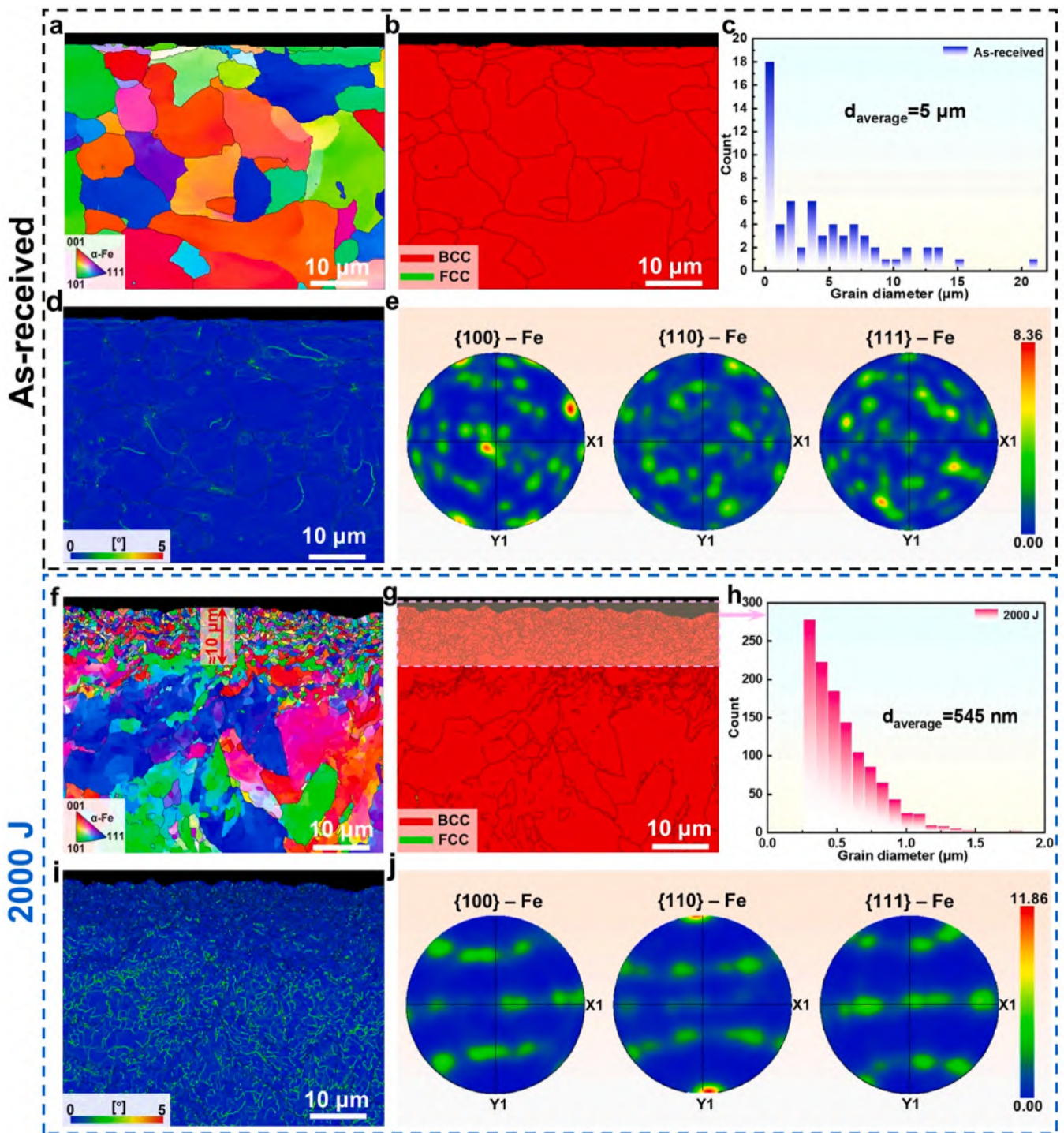


Fig. 8. (a-e) IPF coloring, phase, grain size distribution, KAM maps, and pole figure of the cross-section of the original Q235 steel. (f-j) Corresponding IPF coloring map, phase map, grain size distribution, KAM map, and pole figure of the cross-section of Q235 steel after 2000 J UV treatment.

of quasi-amorphous/amorphous structures within the oxide layer. Overall, the UV method delivers energy via high-frequency vibrations to enhance atomic mobility, meanwhile triggering interfacial or structural transformations and promoting the formation of new phases and species.

3.5. Wear mechanisms before and after ultrasonic vibration treatment

Integrating all the results of the present work, a schematic was constructed to illustrate the evolution of the wear mechanisms in Q235 steel before and after 2000 J UV treatment, as shown in Fig. 11.

In the original state, the original Q235 steel exhibits uniformly distributed coarse grains. After the 2000 J UV treatment, the grain size gradually increases from the surface toward the core, exhibiting a distinct grain refinement feature. Meanwhile, an iron-containing oxide layer forms on the surface, although its thickness is less than that of the grain-refined region. In the stable wear state, the original Q235 steel exhibits deep and broad wear tracks accompanied by distinct edge bulges induced by plastic deformation. Numerous wear debris, peeling, and grooves are observed within the wear track, indicating that the dominant wear mechanism is adhesive wear, accompanied by minor

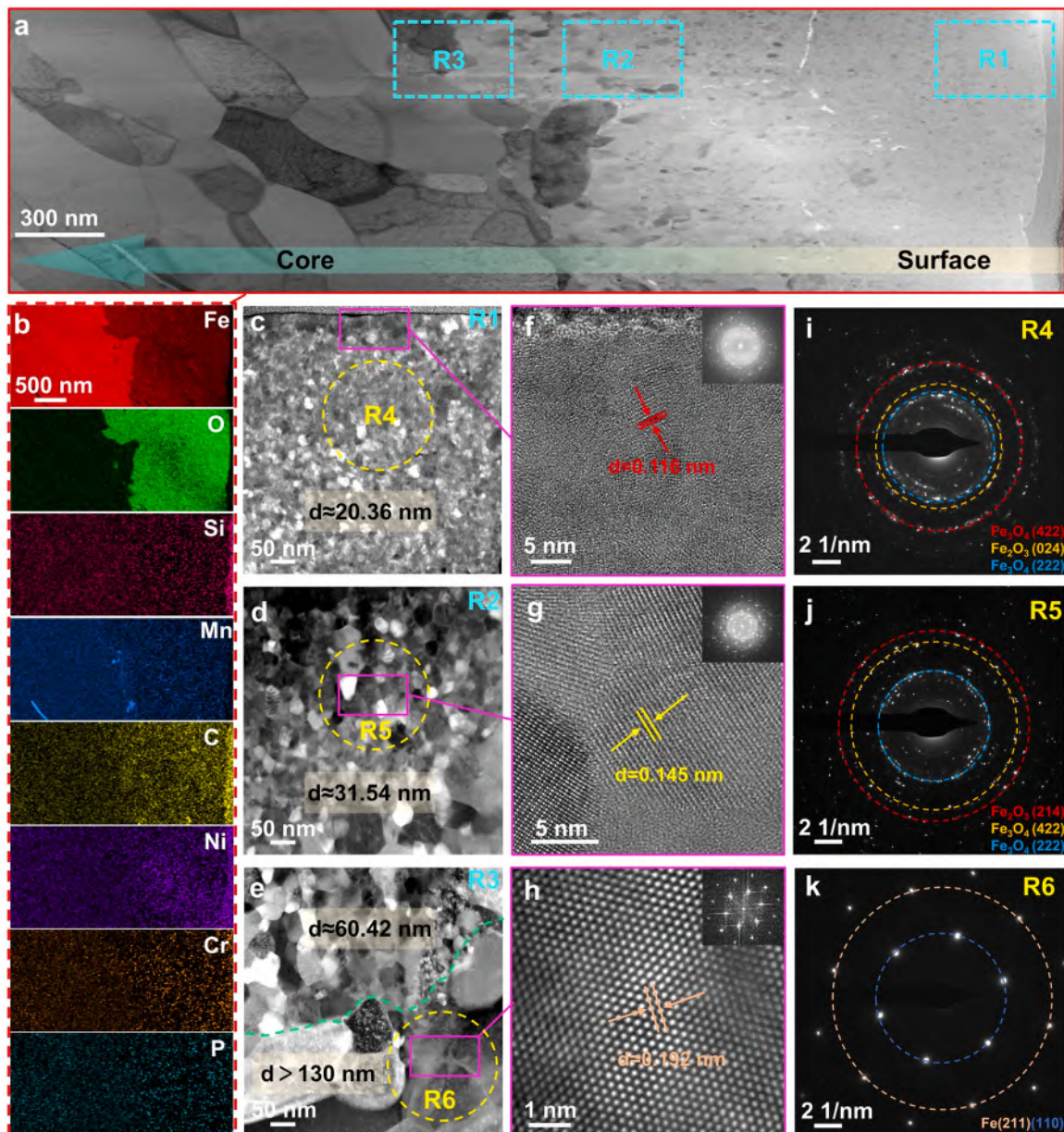


Fig. 9. (a) Cross-sectional TEM image of the Q235 steel sample after 2000 J UV treatment. (b) The EDS results corresponding to (a). (c-e) High-magnification TEM images of the regions labeled R1, R2, and R3 in (a). (f-h) High-resolution TEM images and the corresponding FFT diffraction patterns from the purple-marked regions in (c-e). (i-k) SAED results corresponding to the R4, R5, and R6 regions marked in (c-e).

oxidative, abrasive, and fatigue wear. In contrast, the samples subjected to UV treatment exhibited distinctly shallower and narrower wear tracks without any edge bulging, indicating a significant reduction in plastic deformation. Although a small amount of wear debris remains within the wear track, grooves are scarcely visible, and the amount of peeling is markedly reduced. It is noteworthy that the interior of the wear track on the original samples appears relatively flat and smooth, whereas the treated samples display a serrated morphology with micro-pits produced by brittle spalling. The primary wear mechanism shifts to fatigue wear, accompanied by minor amounts of abrasive, oxidative, and adhesive wear.

As evidenced by the results, UV treatment facilitates the formation of a surface oxide layer and constructs a gradient nanostructure through grain refinement. These alterations significantly improve the material's surface hardness and wear resistance, eventually transforming its wear behavior from plastic deformation to brittle spalling.

4. Conclusion

In this work, a heat-source-free cold manufacturing strategy based on UV surface modification is proposed to significantly enhance the wear resistance of Q235 steel. The samples were subjected to UV treatments with energies of 250, 500, 1000, and 2000 J, resulting in an increase in microhardness from 168.7 HV to 299.8, 359.3, 467.3, and 469.9 HV, respectively. For the 2000 J treated sample, the surface nanohardness increased from 5.52 to 22.34 GPa, with the treatment featuring a low load (< 30 MPa), a mild temperature rise (~ 280.6 °C), and a short duration (< 6 s). Under RT, 50 N, and 100 rpm conditions, the original sample exhibited a wear rate of $13.56 \times 10^{-6} \text{ mm}^3 \text{ N}^{-1} \text{ m}^{-1}$, showing pronounced plastic deformation and adhesive wear. After the 2000 J treatment, the wear rate decreased to $3.02 \times 10^{-6} \text{ mm}^3 \text{ N}^{-1} \text{ m}^{-1}$, with the maximum wear depth reduced from 8.03 μm to 2.67 μm , and the wear mechanism changed to brittle spalling and fatigue wear. The results show that UV treatment not only generates a ~ 1.5 μm thick

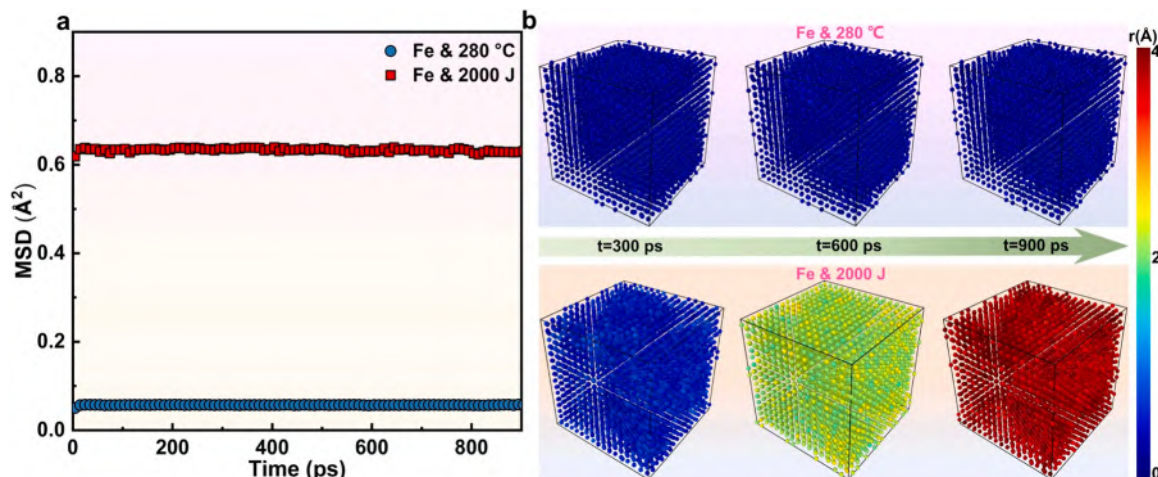


Fig. 10. (a–b) Molecular dynamics simulations of the time evolution of the MSD of Fe atoms under two distinct conditions: thermal treatment at 280 °C and UV at 2000 J, together with trajectory images illustrating the time-dependent displacement of individual Fe atoms in the 3D model.

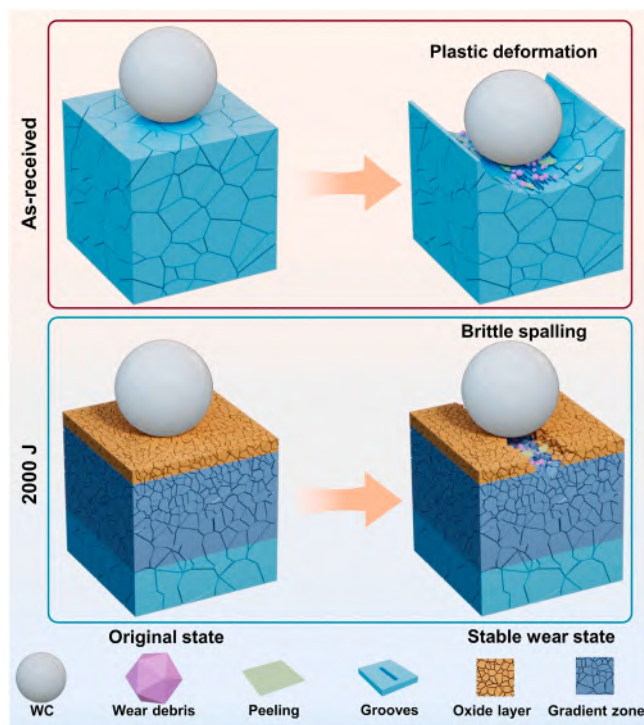


Fig. 11. Schematic illustration of the wear mechanisms of the original Q235 steel and the sample treated with 2000 J UV.

composite oxide layer containing Fe^{2+} and Fe^{3+} on the surface but also induces the formation of a $\sim 10 \mu\text{m}$ gradient nanostructure, thereby enhancing surface hardness and wear resistance. Hence, our results provide an efficient and cost-effective strategy that enables surface property enhancement of steel and other metallic materials under rapid, low-load, and low-temperature-rise conditions, showing significant potential for engineering applications.

CRediT authorship contribution statement

Shike Huang: Writing – review & editing, Writing – original draft, Visualization, Validation, Software, Project administration, Methodology, Investigation, Funding acquisition, Formal analysis, Data curation, Conceptualization. **Xiangyang Yu:** Validation, Supervision,

Investigation. **Shengyu Zhao:** Supervision, Investigation, Formal analysis. **Yihong Yan:** Validation, Supervision, Investigation. **huang Jinbiao:** Validation, Supervision, Investigation. **chen Jianyu:** Supervision, Investigation. **Sajad Sohrabi:** Supervision. **Wenqing Ruan:** Supervision. **Amir Hossein Taghvaei:** Supervision. **Jiang Ma:** Writing – review & editing, Supervision, Resources, Methodology.

Declaration of Competing Interest

The authors declare that they have no known competing financial interests or personal relationships that could have appeared to influence the work reported in this paper.

Acknowledgments

The work was financially supported by the Key-Area Research and Development Program of Guangdong Province (Grant No. 2024B0101070001), the NSF of China (Grant Nos. 52571191, 52401217, 52271150, 52571190), Advanced Materials-National Science and Technology Major Project (Grant No. 2025ZD0619204), the Science, Technology and Innovation Commission of Shenzhen Municipality (Grants No. RCJC20221008092730037, JCYJ20250604182240052, JCYJ20240813141413018). Additionally, this project is supported by the Special Fund for the Cultivation of Independent Innovation Achievements of Postgraduate Students at Shenzhen University (315–00066010722). We thank the Instrumental Analysis Center of Shenzhen University for the assistance with the Electron Microscope.

Data availability

Data will be made available on request.

References

- [1] Xu F, Ding N, Li N, Liu L, Hou N, Xu N, et al. A review of bearing failure Modes, mechanisms and causes. *Eng Fail Anal* 2023;152:107518. <https://doi.org/10.1016/j.engfailanal.2023.107518>.
- [2] Kumar A, Gandhi CP, Zhou Y, Kumar R, Xiang J. Latest developments in gear defect diagnosis and prognosis: A review. *Measurement* 2020;158:107735. <https://doi.org/10.1016/j.measurement.2020.107735>.
- [3] Luo J, Sun W, Liang D, Chan KC, Yang X-S, Ren F. Superior wear resistance in a TaMoNb compositionally complex alloy film via in-situ formation of the amorphous-crystalline nanocomposite layer and gradient nanostructure. *Acta Mater* 2023;243:118503. <https://doi.org/10.1016/j.actamat.2022.118503>.
- [4] Holmberg K, Erdemir A. Influence of tribology on global energy consumption, costs and emissions. *Friction* 2017;5:263–84. <https://doi.org/10.1007/s40544-017-0183-5>.

- [5] Holmberg K, Erdemir A. The impact of tribology on energy use and CO₂ emission globally and in combustion engine and electric cars. *Tribol Int* 2019;135:389–96. <https://doi.org/10.1016/j.triboint.2019.03.024>.
- [6] Holmberg K, Andersson P, Erdemir A. Global energy consumption due to friction in passenger cars. *Tribol Int* 2012;47:221–34. <https://doi.org/10.1016/j.triboint.2011.11.022>.
- [7] Jia Q, He W, Hua D, Zhou Q, Du Y, Ren Y, et al. Effects of structure relaxation and surface oxidation on nanoscopic wear behaviors of metallic glass. *Acta Mater* 2022; 232:117934. <https://doi.org/10.1016/j.actamat.2022.117934>.
- [8] Zhang S-w. Green tribology: Fundamentals and future development. *Friction* 2013; 1:186–94. <https://doi.org/10.1007/s40544-013-0012-4>.
- [9] Sun F, Deng S, Fu J, Zhu J, Liang D, Wang P, et al. Superior high-temperature wear resistance of an Ir-Ta-Ni-Nb bulk metallic glass. *J Mater Sci Technol* 2023;158: 121–32. <https://doi.org/10.1016/j.jmst.2023.02.040>.
- [10] Huang S, Sun F, Sun R, Zhu L, Huang J, Zhao S, et al. Micro- and nanoscale glass compression molding using the metallic glass mold. *J Mater Sci Technol* 2026;249: 230–41. <https://doi.org/10.1016/j.jmst.2025.05.073>.
- [11] Yang W, Li Q, Liu W, Liang J, Peng Z, Liu B. Characterization and properties of plasma electrolytic oxidation coating on low carbon steel fabricated from aluminate electrolyte. *Vacuum* 2017;144:207–16. <https://doi.org/10.1016/j.vacuum.2017.08.003>.
- [12] Fenili CP, de Souza FS, Marin G, Probst SMH, Binder C, Klein AN. Corrosion resistance of low-carbon steel modified by plasma nitriding and diamond-like carbon. *Diam Relat Mater* 2017;80:153–61. <https://doi.org/10.1016/j.diamond.2017.11.001>.
- [13] Yan M, Sun J-n, Huang H-g, Chen L, Dong K, Chen Z-y. Effect of hot rolling and cooling process on microstructure and properties of 2205/Q235 clad plate. *J Iron Steel Res Int* 2018;25:1113–22. <https://doi.org/10.1007/s42243-018-0172-6>.
- [14] Rai PK, Shekhar S, Mondal K. Effects of grain size gradients on the fretting wear of a specially-processed low carbon steel against AISI E52100 bearing steel. *Wear* 2018;412–413:1–13. <https://doi.org/10.1016/j.wear.2018.07.014>.
- [15] Wang B, Xue W, Wu J, Jin X, Hua M, Wu Z. Characterization of surface hardened layers on Q235 low-carbon steel treated by plasma electrolytic borocarbonizing. *J Alloy Compd* 2013;578:162–9. <https://doi.org/10.1016/j.jallcom.2013.04.153>.
- [16] Yang Z, Liang W, Miao Q, Ding Z, Zuo S. Tribological behavior of borocarbonized layer on low-carbon steel treated by double glow plasma surface alloying. *Mater Res Express* 2020;7:066404. <https://doi.org/10.1088/2053-1591/ab9980>.
- [17] Wang B, Jin X, Xue W, Wu Z, Du J, Wu J. High temperature tribological behaviors of plasma electrolytic borocarbonized Q235 low-carbon steel. *Surf Coat Technol* 2013;232:142–9. <https://doi.org/10.1016/j.surfcoat.2013.04.064>.
- [18] Zhang Z, Wang D, Liu G, Qian Y, Xu Y, Xiang D. Surface modification of 42CrMo steels: a review from wear and corrosion resistance. *Coatings* 2024;14:337. <https://doi.org/10.3390/coatings14030337>.
- [19] Ji W, Zhou R, Vivegananthan P, See Wu M, Gao H, Zhou K. Recent progress in gradient-structured metals and alloys. *Prog Mater Sci* 2023;140:101194. <https://doi.org/10.1016/j.pmatsci.2023.101194>.
- [20] Zhang Y, Liang F, Lin Y, Chen X, Zhu Y. Mitigating friction and wear by pre-designed or tribo-induced heterostructures: an overview. *Mater Res Lett* 2024;12: 535–50. <https://doi.org/10.1080/21663831.2024.2356282>.
- [21] Liu R, Yuan S, Lin N, Zeng Q, Wang Z, Wu Y. Application of ultrasonic nanocrystal surface modification (UNSM) technique for surface strengthening of titanium and titanium alloys: a mini review. *J Mater Res Technol* 2021;11:351–77. <https://doi.org/10.1016/j.jmrt.2021.01.013>.
- [22] Yuan S, Lin N, Zeng Q, Zhang H, Liu X, Wang Z, et al. Recent developments in research of double glow plasma surface alloying technology: a brief review. *J Mater Res Technol* 2020;9:6859–82. <https://doi.org/10.1016/j.jmrt.2020.03.123>.
- [23] Sun H, Song B, Sun X, Cui X, Liu Z, Cong M, et al. Recent representative progress of surface coating technology. *Chem Rec* 2025;25:e202500054. <https://doi.org/10.1002/trc.202500054>.
- [24] Guo Z, Guo B, Zhao Q, Zeng Z, Xu L. Wear characteristics of micro-structured CVD diamond grinding tools. *Wear* 2023;514–515:204569. <https://doi.org/10.1016/j.wear.2022.204569>.
- [25] Liu X, Bi J, Meng Z, Li R, Li Y, Zhang T. Tribological behaviors of high-hardness Co-based amorphous coatings fabricated by laser cladding. *Tribol Int* 2021;162: 107142. <https://doi.org/10.1016/j.triboint.2021.107142>.
- [26] Zhang E, Zhang Z, Jing Z, Yuan J, Ma C, Yan S, et al. Research progress on process optimization of thermal-sprayed iron-based amorphous coatings. *Integr Mater Manuf Innov* 2025;14:247–75. <https://doi.org/10.1007/s40192-025-00408-3>.
- [27] Wang J, Li Z, Wang D, Qiu S, Ernst F. Thermal stability of low-temperature-carbonized austenitic stainless steel. *Acta Mater* 2017;128:235–40. <https://doi.org/10.1016/j.actamat.2017.02.018>.
- [28] Wang Y, Yang Y, Yang H, Zhang M, Qiao J. Effect of nitriding on the tribological properties of Al_{1.3}CoCuFeNi₂ high-entropy alloy. *J Alloy Compd* 2017;725:365–72. <https://doi.org/10.1016/j.jallcom.2017.07.132>.
- [29] Dalke A, Burlacov I, Spies H-J, Biermann H. Use of a solid carbon precursor for DC plasma nitrocarburizing of AISI 4140 steel. *Vacuum* 2018;149:146–9. <https://doi.org/10.1016/j.vacuum.2017.12.033>.
- [30] Liu Y, Yang Y, Chen C. Microstructure and properties of Ni-Ti based gradient laser cladding layer of Ti₆Al₄V alloy by laser powder bed fusion. *Addit Manuf* 2024;79: 103906. <https://doi.org/10.1016/j.addma.2023.103906>.
- [31] Yang Z, Liang W, Jia Y, Miao Q, Ding Z, Yu H. High temperature tribological behavior of borocarbonized layer on Q235 Steel. *Mater Sci* 2021;27:42–9. <https://doi.org/10.5755/j02.ms.24682>.
- [32] Chen Y, Zhang H, Wang B, Huang J, Zhou M, Wang L, et al. A review of research on improving wear resistance of titanium alloys. *Coatings* 2024;14:786. <https://doi.org/10.3390/coatings14070786>.
- [33] Yue X, Du H, Zhang L, Hou L, Wang Q, Wei H, et al. Grain gradient refinement and corrosion mechanisms in metals through severe plastic deformation: insights from Surface Mechanical Attrition Treatment (SMAT). *Adv Compos Hybrid Mater* 2025; 8:122. <https://doi.org/10.1007/s42114-024-01167-z>.
- [34] Li WL, Tao NR, Lu K. Fabrication of a gradient nano-micro-structured surface layer on bulk copper by means of a surface mechanical grinding treatment. *Scr Mater* 2008;59:546–9. <https://doi.org/10.1016/j.scriptamat.2008.05.003>.
- [35] Huang HW, Wang ZB, Lu J, Lu K. Fatigue behaviors of AISI 316L stainless steel with a gradient nanostructured surface layer. *Acta Mater* 2015;87:150–60. <https://doi.org/10.1016/j.actamat.2014.12.057>.
- [36] Kumar S, Sudhakar Rao G, Chattopadhyay K, Mahobia GS, Santhi Srinivas NC, Singh V. Effect of surface nanostructure on tensile behavior of superalloy IN718. *Mater Des* 2014;62:76–82. <https://doi.org/10.1016/j.matdes.2014.04.084>.
- [37] Amanov A, Yeo IK, Jeong SH. Advanced post-processing of Ti-6Al-4V alloy fabricated by selective laser melting: A study of laser shock peening and ultrasonic nanocrystal surface modification. *J Mater Res Technol* 2025;35:4020–31. <https://doi.org/10.1016/j.jmrt.2025.02.038>.
- [38] Ren Y, Wan H, Chen Y, Zhu H, Lu H, Ren X. Effect of laser shock peening and carbonitriding on tribological properties of 20Cr2Mn2Mo steel alloy under dry sliding conditions. *Surf Coat Technol* 2021;417:127215. <https://doi.org/10.1016/j.surfcoat.2021.127215>.
- [39] Chan HL, Ruan HH, Chen AY, Lu J. Optimization of the strain rate to achieve exceptional mechanical properties of 304 stainless steel using high speed ultrasonic surface mechanical attrition treatment. *Acta Mater* 2010;58:5086–96. <https://doi.org/10.1016/j.actamat.2010.05.044>.
- [40] Ren XD, Zhou WF, Liu FF, Ren YP, Yuan SQ, Ren NF, et al. Microstructure evolution and grain refinement of Ti-6Al-4V alloy by laser shock processing. *Appl Surf Sci* 2016;363:44–9. <https://doi.org/10.1016/j.apsusc.2015.11.192>.
- [41] Lu YJ, Ma SY, Zhang JG, Xiao JF, Chen X, Xu JF. Investigation on the microstructure variation of LZ91 Mg-Li alloy by ultrasonic nanocrystal surface modification. *J Alloy Compd* 2025;1021:179706. <https://doi.org/10.1016/j.jallcom.2025.179706>.
- [42] Xu W, Liu XC, Lu K. Strain-induced microstructure refinement in pure Al below 100 nm in size. *Acta Mater* 2018;152:138–47. <https://doi.org/10.1016/j.actamat.2018.04.014>.
- [43] Liu RY, Yuan S, Lin NM, Zeng QF, Wang ZH, Wu YC. Application of ultrasonic nanocrystal surface modification (UNSM) technique for surface strengthening of titanium and titanium alloys: a mini review. *J Mater Res Technol* 2021;11:351–77. <https://doi.org/10.1016/j.jmrt.2021.01.013>.
- [44] Li H, Li X, Jin C, Li Q, Ma Q, Hua K, et al. Mechanical and tribological performance of AlCr_{0.5}NbTa_xTi_{4-x} (x=0, 0.5, 1) refractory high-entropy alloys. *J Mater Sci Technol* 2023;156:241–53. <https://doi.org/10.1016/j.jmst.2023.02.016>.
- [45] Mi G, Xiong L, Wang C, Hu X, Wei Y. A thermal-metallurgical-mechanical model for laser welding Q235 steel. *J Mater Process Technol* 2016;238:39–48. <https://doi.org/10.1016/j.jmatprotec.2016.07.002>.
- [46] Zhang Y, Wang W, Xiao Y, Ma J. Improvement of corrosion-wear resistance of Zr-based metallic glass by pre-oxidation treatment. *Intermetallics* 2025;185:108897. <https://doi.org/10.1016/j.intermet.2025.108897>.
- [47] Wang W, Sun F, Zhang H, Huang J, Yu X, Ma J. Improvement of high-temperature wear resistance of Zr-based metallic glass by pre-oxidation treatment. *J Mater Res Technol* 2024;29:2166–74. <https://doi.org/10.1016/j.jmrt.2024.01.169>.
- [48] Li Y, Liu Y, Zhan Y, Zhang Y, Zhao X, Yang M, et al. Peracetic acid-induced nanoengineering of Fe-based metallic glass ribbon in application of efficient drinking water treatment. *Appl Catal B Environ Energy* 2024;355:124161. <https://doi.org/10.1016/j.apcatb.2024.124161>.
- [49] Jiang W, Zhou J, Cao Y, Meng A, Liu R, Li J, et al. Tribo-induced microstructural evolutions and wear mechanisms of AlCoCrFeNi_{2.1} eutectic high-entropy alloy at elevated temperatures. *Acta Mater* 2025;296:121272. <https://doi.org/10.1016/j.actamat.2025.121272>.
- [50] Tong WP, Tao NR, Wang ZB, Lu J, Lu K. Nitriding iron at lower temperatures. *Science* 2003;299:686–8. <https://doi.org/10.1126/science.1080216>.
- [51] Zhu YT, Ameyama K, Anderson PM, Beyerlein IJ, Gao HJ, Kim HS, et al. Heterostructured materials: superior properties from hetero-zone interaction. *Mater Res Lett* 2021;9:1–31. <https://doi.org/10.1080/21663831.2020.1796836>.
- [52] Sun WB, Li HJ, Xiao CY, Wang JB, Si CR. Effect of surface nanocrystallization on the microstructural evolution and wear resistance of low-temperature nitrided SLM-TC4 Alloy. *Tribol Int* 2026;216:111516. <https://doi.org/10.1016/j.triboint.2025.111516>.
- [53] Jiang J, Ruan W, Zeng S, Lin J, Zhao X, Fu J, et al. Self-supported partially crystallized nanoporous metallic glass for ultra-stable and efficient electrocatalytic

- hydrogen evolution. *Sci China Mater* 2026. <https://doi.org/10.1007/s40843-025-3506-3>.
- [54] Li L, Zhang Y, Huang J, Chen Z, Yu X, Li Wei, et al. Cold manufacturing of metallic glass-based composites by ultrasonic vibrations. *J Mater Process Technol* 2026; 348:119178. <https://doi.org/10.1016/j.jmatprotec.2025.119178>.
- [55] Zhang Z, Liang D, Tang G, Hua Y, Dong B, Liang Z. Data-driven multi-objective synergistic to targeted enhancement framework for high-performance aluminum alloy design. *Eng Appl Artif Intell* 2026;165:113474. <https://doi.org/10.1016/j.engappai.2025.113474>.
- [56] Liang Z, Dou W, Zhao Z, Ran L, Lin A, Zou T, et al. Improved wear resistance of Ti-6Al-4 V alloy by fabricating a SiC/Co composite layer through ultrasonic strengthening grinding process. *Results Eng* 2026;29:108881. <https://doi.org/10.1016/j.rineng.2025.108881>.
- [57] Liang Z, Cheng Z, Hua Y, Yu X, Tan G, Huang X, et al. TiC-induced grain refinement and second-phase strengthening enhancing wear resistance of SLM-processed CoCrFeNi high-entropy alloys. *J Alloys Compd* 2025;1041:183897. <https://doi.org/10.1016/j.jallcom.2025.183897>.
- [58] Tang G, Ou Z, Liu F, Li T, Su F, Zheng J, et al. Enhancing wear resistance of aluminum alloy by fabricating a Ti-Al modified layer via surface mechanical attrition treatment. *Tribol Int* 2024;193:109462. <https://doi.org/10.1016/j.triboint.2024.109462>.